SCIEPublish

Article

Additive Manufacturing of Tungsten-Alloyed Tantalum from Polyhedral Shaped Powder Blends

Silja-Katharina Rittinghaus [1,*], Markus Benjamin Wilms [1], Fengxiang Lin [2], Dimitrios Nikas [2], Janett Schmelzer [3] and Pavel Krakhmalev [2]

[1] Chair of Materials Science and Additive Manufacturing, School of Mechanical Engineering and Safety Engineering, University of Wuppertal, Gaußstr. 20, 42119 Wuppertal, Germany; markusbenjamin.wilms@boschrexroth.de (M.B.W.)

[2] Department of Engineering and Physics, Karlstad University, 651 88 Karlstad, Sweden; fengxiang.lin@kau.se (F.L.); dimitrios.nikas@kau.se (D.N.); pavel.krakhmalev@kau.se (P.K.)

[3] Institute for Materials and Joining Technology, Faculty of Mechanical Engineering Otto von Guericke University of Magdeburg, Universitätsplatz 2, 39106 Magdeburg, Germany; j.schmelzer@solar-materials.com (J.S.)

* Corresponding author. E-mail: rittinghaus@uni-wuppertal.de (S.-K.R.)

Received: 8 February 2025; Accepted: 14 March 2025; Available online: 21 March 2025

ABSTRACT: Tantalum and tungsten are completely soluble in each other and are used in applications in the combined form of so-called tantaloys. They provide high melting points (Ta: 3017 °C, W: 3410 °C) and excellent corrosion resistance while maintaining high ductility for W contents up to 7.5 wt%. Providing good resistance to hydrogen embrittlement, Ta-W alloys are attractive candidates for applications in fusion reactors. This study demonstrated the feasibility of producing chemically homogeneous bulk material with fine grained microstructure from non-spherical powder blends with up to 7.5% tungsten using laser powder bed fusion (PBF-L/M). It is observed that cracking remains a challenge, especially with the increase in tungsten content. The effect of rapid solidification on the microhardness of up to 385 HV0.1 for 7.5% W is discussed. It provides initial indications of the possibility of achieving higher strengths and paves the way for further alloy development with regard to the additive manufacturing of this alloy family.

Keywords: Additive Manufacturing; Tantalum; Tantaloy; Refractory metals

1. Introduction

Refractory metals are essential for diverse high-temperature applications and thus are increasingly considered for components in highly efficient propulsion engines, power plants and the chemical industry. Tantalum has gained particular interest [1–7] because of its high-temperature stability and the ability to form a native Ta_2O_5 oxide layer for improved corrosion resistance towards aggressive gaseous and liquid media [8,9]. Moreover, tantalum is known for its excellent biocompatibility, particularly pure tantalum. Thus, pure tantalum is mainly used for medical parts, e.g., scaffolds [10–13]. Conventionally, tantalum and its alloys are manufactured by sintering techniques [14–17] or electron beam furnaces [18]. Recently, additive manufacturing of refractory metals, e.g., tungsten [19–23], molybdenum [24–27] and niobium [28,29] has been successfully demonstrated in various studies. Additive manufacturing (AM) of pure tantalum has been explored using PBF-LB/M [30–37], PBF-EB/M [38,39] and directed energy deposition techniques [40,41] or cold gas deposition technologies [42].

However, applications in structural components typically demand higher strength, which can be achieved by alloying with tungsten, forming a bcc-structured solid solution strengthened alloy [43,44]. These Ta-W alloys, also referred to as tantaloy, were developed in the 1950s for rocket components [45], but today also find application in the chemical- and marine industry, particularly for vacuum-proof components and parts exposed to highly aggressive chemicals [15], e.g., chlorine environments [46]. Alloys from the tantaloy family offer high-temperature stability with high strength and high ductility in ambient and elevated temperature regimes [17,47,48] without deterioration of the corrosion resistance compared to pure tantalum [49] or sensitivity to hydrogen embrittlement [50]. Hence, Ta-W alloys

https://doi.org/10.70322/htm.2025.10005

are currently considered for applications in future fusion reactors [47,51]. Current research in the context of rapid solidification focuses on Ta-10W (wt%) [52,53], while despite very interesting property profiles, to our best knowledge, no study on additive manufacturing of materials <10 wt% W has been performed which could greatly benefit from both increased strength through fine-grained microstructures and near net shape production provided by these group of processes. Furthermore, most studies focus on spherical atomized powders, which represent a significant cost factor for the use of additive manufacturing.

Consequently, in this work, laser powder bed fusion (PBF-L/M) with W content varied 0–7.5 wt% in orientation to tantaloy 63 (Ta-2.5W) and 61 (Ta-7.5W) is experimentally studied. Due to the material's high melting point and reactivity, atomized powders are costly. Therefore, this study explores the feasibility of producing Ta-W powders suitable for AM through mechanical alloying and investigates the potential for fabricating bulk material using PBF-LB/M from these polyhedral powders. Furthermore, the research examines how the variation in tungsten content influences the microstructure and microhardness of the resulting bulk samples. The overarching goal of this study is to enhance the understanding of how tantalum alloys can be effectively utilized in additive manufacturing (AM) to produce high-performance components with optimized properties while ensuring both economic feasibility and sustainability through the use of low-cost feedstock materials.

2. Materials and Methods

This study used various materials and methods to address the outlined research questions. The experiments represent initial feasibility studies and were conducted under laboratory conditions on a small scale. The materials and procedures employed are described below. The key steps for material processing are depicted in Figure 1 and explained in the following paragraphs.

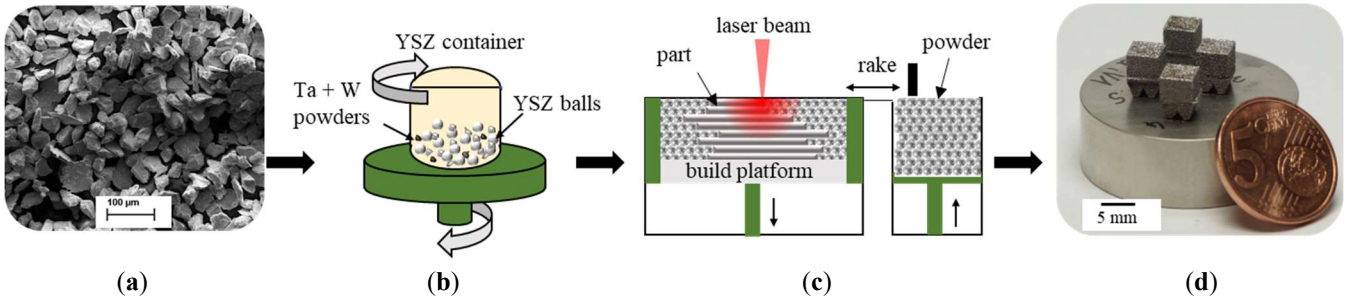

Figure 1. Overview of key processing steps in this study: (**a**) Initial powder feedstock, schematic overview of the (**b**) mechanical alloying and (**c**) PBF-LB/M process applied in this study, (**d**) actual samples produced by the process (here: Ta reference).

2.1. Materials

The powder material used was pure tantalum (Ta, 99.9%) with a specified particle size of <75 µm (Goodfellow GmbH, Hamburg, Germany) and particle sizes measured as D90 = 55.1 µm, D50 = 41 µm, and D10 = 18.9 µm. Tungsten (W) powder with a purity of 99.9% and a nominal size of <45 µm (H.C. Starck, Goslar, Germany) was used as an additive. D90, D50 and D10 were measured to be 43.8 µm, 5.8 µm and 4.1 µm, respectively. According to the manufacturer's specifications, both powders were produced using a mechanical grinding process, resulting in non-spherical, polyhedral-shaped particles. As substrate material, stainless steel (1.4404) was used.

2.2. Processing

2.2.1. Mechanical Alloying

Mechanical alloying was performed in a Fritsch Pulverisette 4 Classic line (Fritsch GmbH, Idar-Oberstein, Germany) using milling containers and milling balls (diameter: 5 mm), both manufactured from YSZ (yttrium stabilized zirconia). Prior to mechanical alloying, a full argon atmosphere was established inside the milling containers to prevent extensive oxidation of the manually mixed powder materials. Each of the subsequent three milling intervals of 20 min was followed by pausing the process for cooling for 10 min. A rotational speed of 100 rpm was selected for both the main and planetary discs. The ball-to-powder ratio was 5:1, and 100 g of powder was milled per batch. After milling, the powders were immediately transferred to the PBF-L/M setup and processed to minimize oxygen pickup during powder handling.

2.2.2. Additive Manufacturing PBF-L/M

The experiments were performed using an experimental lab setup, consisting of a single mode fiber laser YLR1000WC, P_{max} = 1 kW, λ = 1070 nm (IPG Photonics GmbH, Burbach, Germany) as an energy source, a HurrySCAN20 (SCANLab GmbH, Puchheim, Germany) galvano scanner, and an f-theta lens (f = 255 mm). The resulting spot diameters were approx. 80 µm in the focal plane. The PBF-L/M process was performed under a full argon atmosphere (Ar 4.6 (99.996% purity), residual O < 10 ppm) and an overpressure of approx. 60 mbar compared to ambient pressure. The investigated samples with a size of approx. 5 mm × 5 mm × 5 mm (Figure 1d) were selected from a parameter study in which the scan speed was varied between 300 and 500 mm/s to achieve the highest possible density in each build. The corresponding final process parameters are listed in Table 1.

Table 1. PBF-LB/M process parameters used in this study.

Process Parameter	Ta	Ta-2.5W (wt%)	Ta-5W (wt%)	Ta-7.5W (wt%)
Laser power [W]			300	
Beam diameter [µm]			80	
Hatch distance [µm]			120	
Layer height [µm]			30	
Scan speed [mm/s]		400		450

2.3. Analytical Methods

2.3.1. Powder Particle Analysis

Powders were analyzed using a SEM LEO 1455 EP (Carl Zeiss AG, Oberkochen, Germany). The particle size distribution was measured using dynamic image analysis with the Helos/Br + Oasis/L + Vibri/L laser diffraction (LD) system (Sympatec GmbH, Königsbrunn, Germany). Particle diameters were determined using the EQPC method, which calculates the diameter of a circle that has the same area as the particle being measured.

2.3.2. Microstructure

Sample preparation for microstructure analysis consisted of standard metallographic grinding and polishing steps. The relative density of specimens was determined using the open-source software ImageJ (Version 1.54) by analyzing the grayscale values of light-optical images obtained at 25× magnification. Cracks were manually excluded from the measurements. Initial SEM imaging of bulk samples was done with a Scios 2 DualBeam (Thermo Fisher Scientific Inc., Waltham, MA, USA). EBSD measurements were performed on ion polished samples using a FE-SEM JEOL JSM-7900 F (JEOL Ltd., Akishima, Japan) equipped with an EBSD C-Nano-detector (Oxford Instruments PLC, Abingdon, UK). EDS measurements were performed both using an EDAX system (AMETEK Inc., Berwyn, IL, USA) and EDS X-MaxN Silicon Drift-detector with Aztec software (Oxford Instruments PLC, Abingdon, VA, USA), respectively. Phase analysis by XRD was conducted using an Empyrean X-ray diffractometer (Malvern Panalytical GmbH, Kassel, Germany) with Cu Kα radiation.

2.3.3. Microhardness

Vickers microhardness was determined using a semi-automatic Vickers tester Carat 930 (ATM Qness GmbH, Mammelzen, Germany). The applied test load was 100 g, and the testing time was 10 s for each indent. The points of the measurement grid were selected manually to ensure testing crack and defect free regions with a minimum distance of 0.23 mm between indents, ensuring a minimum of 24 indents per sample.

3. Results

3.1. Powder Characterization

The initially rough surface and polyhedral particle morphology of the tantalum powder (Figure 2a) changes during the mechanical alloying process, leading to fracturing and slight rounding of the powder particles as the corners are worn down due to pressure and abrasion. The milled powders are also characterized by submicron flakes from both materials, which adhere to larger particles and form occasional, randomly distributed agglomerates (Figure 2b). Based on surface observations, it is assumed that partial cold-welding of the fine tungsten particles (around 10 µm) and mixed

flakes takes place. As the tungsten content increases, the overall particle size decreases slightly (Figure 2c), which can be attributed to the smaller size of the tungsten (<45 µm) and fractured particles compared to the Ta-base powder.

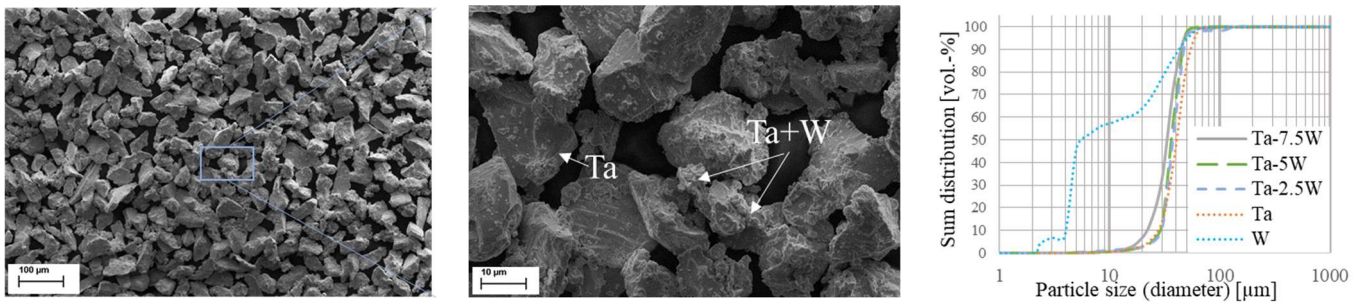

(**a**) (**b**) (**c**)

Figure 2. Exemplary SEM images (SE, obtained at (**a**) low, 1kx and (**b**) high, 5kx magnification) of the mechanically alloyed Ta-7.5W powder and (**c**) results from particle size analysis for all powders processed in this study.

3.2. Microstructure

While both pure Ta and Ta-2.5W (Figure 3a,b) could be manufactured almost crack free, with cracks only being found at isolated singular defects, the Ta-5W and Ta-7.5W materials showed severe cracking (Figure 3c,d). Occurring odd-shaped defects in all samples can be attributed to e.g., irregularities in the powder spread due to the disadvantageous particle shape (Figure 1). The Ta-5W showed more defects and crack formation compared to the samples with lower tungsten content. Sparsely found inclusions could be observed in the cross-sections of the samples. The higher W concentration likely leads to changes in the material's microstructure, such as alterations in the lattice structure and solidification behavior. An increased hardness of the material with higher W content would also reduce its ability to absorb internal stresses caused by shrinking through plastic deformation, making it more susceptible to crack formation. In the parameter variation at 7.5 wt% W, an increase in scan speed from 400 to 450 mm/s seemed to reduce crack formation slightly. This could be due to the formation of smaller melt pools, which allow for more controlled solidification and potentially lower residual stresses, thus reducing the risk of cracks. However, this was not observed for the other samples, and the higher number of defects in the 5 wt% W sample may also represent statistical variations, which could not be further detailed due to the limited sample size. Overall, a higher tungsten content seems to correlate strongly with an increased tendency for crack formation. Nevertheless, the samples reached densities of over 99.5%, with the number of defects increasing as the tungsten content was raised. The relative densities were determined by excluding crack structures as 99.9% for Ta, 99.8% for Ta-2.5W, and 99.5% for Ta-5W and Ta-7.5W, respectively.

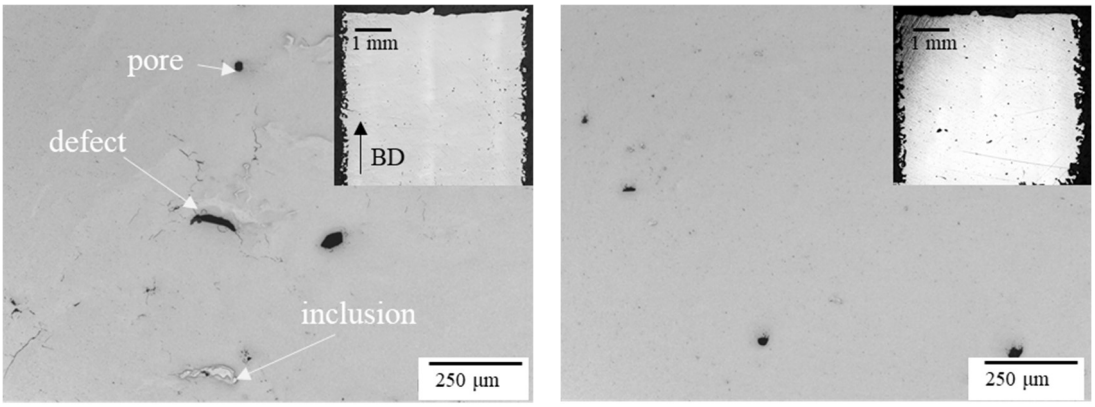

(**a**) (**b**)

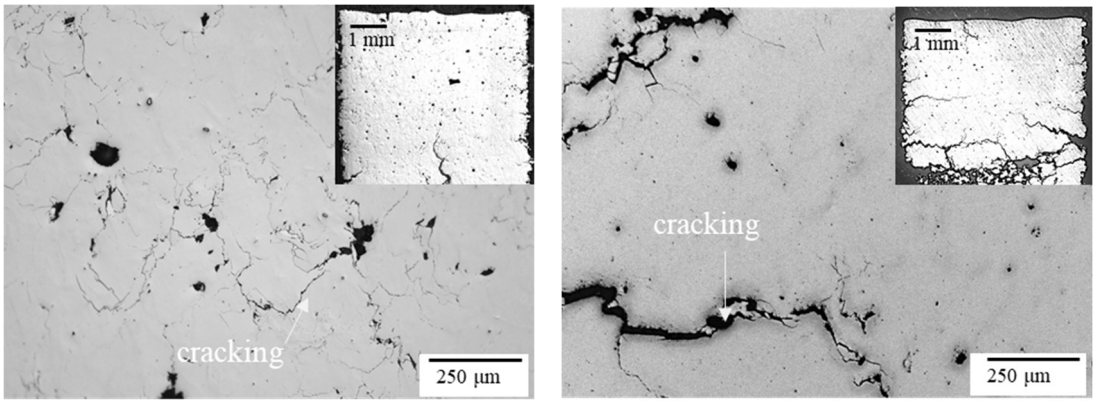

(**c**) (**d**)

Figure 3. LM images (200×) of the PBF-LB/M samples: (**a**) pure Ta, (**b**) Ta-2.5W, (**c**) Ta-5W, (**d**) Ta-7.5W. Respective insets show an overview of the total cross-section. BD = build direction.

The SEM images (Figure 4) revealed a homogeneous microstructure of a presumably single-phase solid solution. No obvious secondary phases were visible, suggesting a single-phase structure. However, previously observed defects and microporosity were again evident within the microstructure, specifically in Figure 4a,b, which may appear similar to potential oxide phases and which were considered during further analysis.

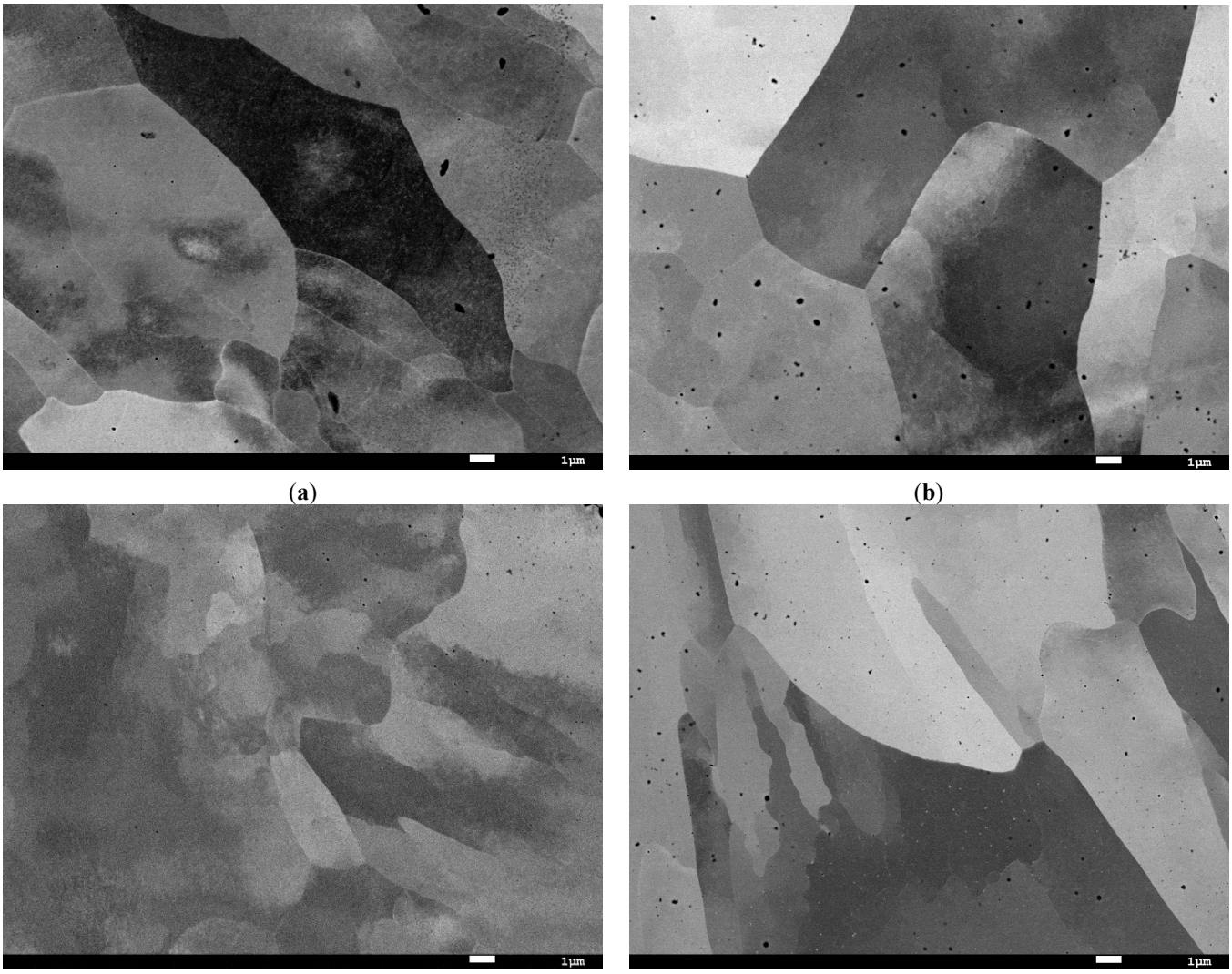

(**a**) (**b**)

(**c**) (**d**)

Figure 4. SEM images (SE) of the PBF-LB/M samples: (**a**) pure Ta, (**b**) Ta-2.5W, (**c**) Ta-5W, (**d**) Ta-7.5W.

EDS measurements confirmed that the W was predominantly homogeneously distributed in the solid solution (Figure 5). Ta-oxide inclusions were detected in small numbers in all samples, as shown in Figure 5a,b. Throughout the

cross sections of approx. 5 mm × 5 mm each, a few W-enriched regions could be determined in the Ta-2.5 (Figure 5c) Ta-5W and Ta-7.5W samples. By further point analyses of the oxygen-rich inclusions, the oxide particles are identified as Ta_2O_5 compounds, as the determined ratios of the chemical concentration (Ta: 79.9 ± 2 wt%, O: 17.1 ± 2 wt%, residual 3 ± 2 wt%) align well with Ta_2O_5 composition.

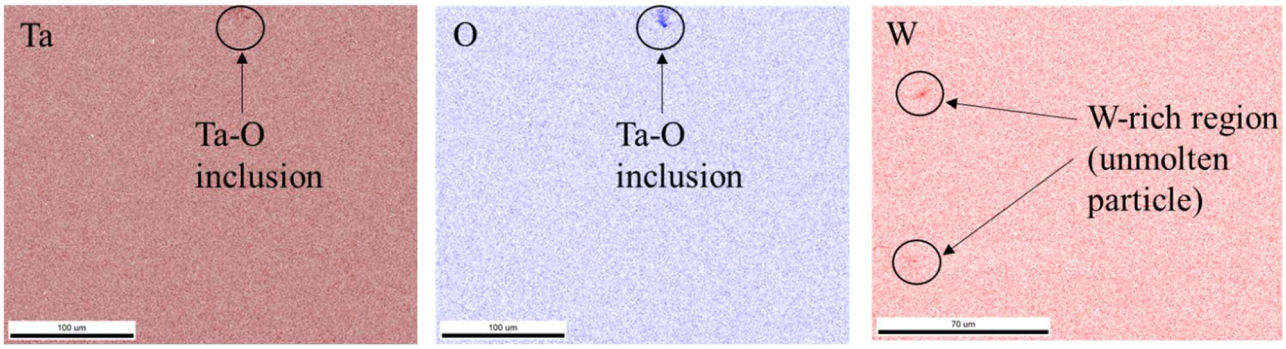

(**a**) (**b**) (**c**)

Figure 5. EDS maps of the PBF-LB/M samples pure Ta (**a**,**b**) and Ta-2.5W (**c**) for the indicated elements for the representation of the occurrence of oxides and unmolten tungsten particles.

The measurement of the overall chemical composition in cross-sections (Table 2) showed that the 2.5W sample contains approximately 2.5 wt% tungsten, while the tungsten content in the solid solution of the 5 wt% and 7.5 wt% samples is slightly lower than intended (4.8 and 6.2 wt%, respectively).

Table 2. Chemical composition determined per EDS using small area scans (10 per sample). Min. and max. values are included as a range in brackets. Values missing up to 100% are attributed to impurities.

Content	Ta (wt%)	Ta-2.5W (wt%)	Ta-5W (wt%)	Ta-7.5W (wt%)
Ta (wt%)	95.2 ± 0.6 (93.7–96.7)	95.8 ± 0.7 (91.2–94.6)	90.9 ± 0.7 (90.0–92.5)	88.8 ± 0.7 (84.9–90.7)
W (wt%)	0.4 ± 0.5 (0.0–0.9)	2.3 ± 0.5 (1.7–3.2)	4.2 ± 0.5 (3.3–5.7)	6.2 ± 0.5 (5.1–9.6)

In all inverse pole figures from EBSD measurements obtained (Figure 6), no pronounced columnar grain structure could be observed. Instead, the microstructure predominantly shows equiaxed grains. This indicates that the material has a relatively uniform grain structure with no significant directional growth, suggesting an isotropic distribution of the crystallographic orientations. Both visually large and small grains are statistically distributed in all samples, and no correlation can be deduced with the scan pattern or melt pool boundaries. EBSD analysis also indicates that the observed cracks (Figure 6, black arrows) develop along grain boundaries.

Grain statistics derived from EBSD maps by setting the threshold for individual grains at 10° and taking into account the equivalent circle diameter (ECD) of the individual reconstructed grains are presented in Figure 7. To allow for more representative quantification, measurements for two sites per sample were merged.

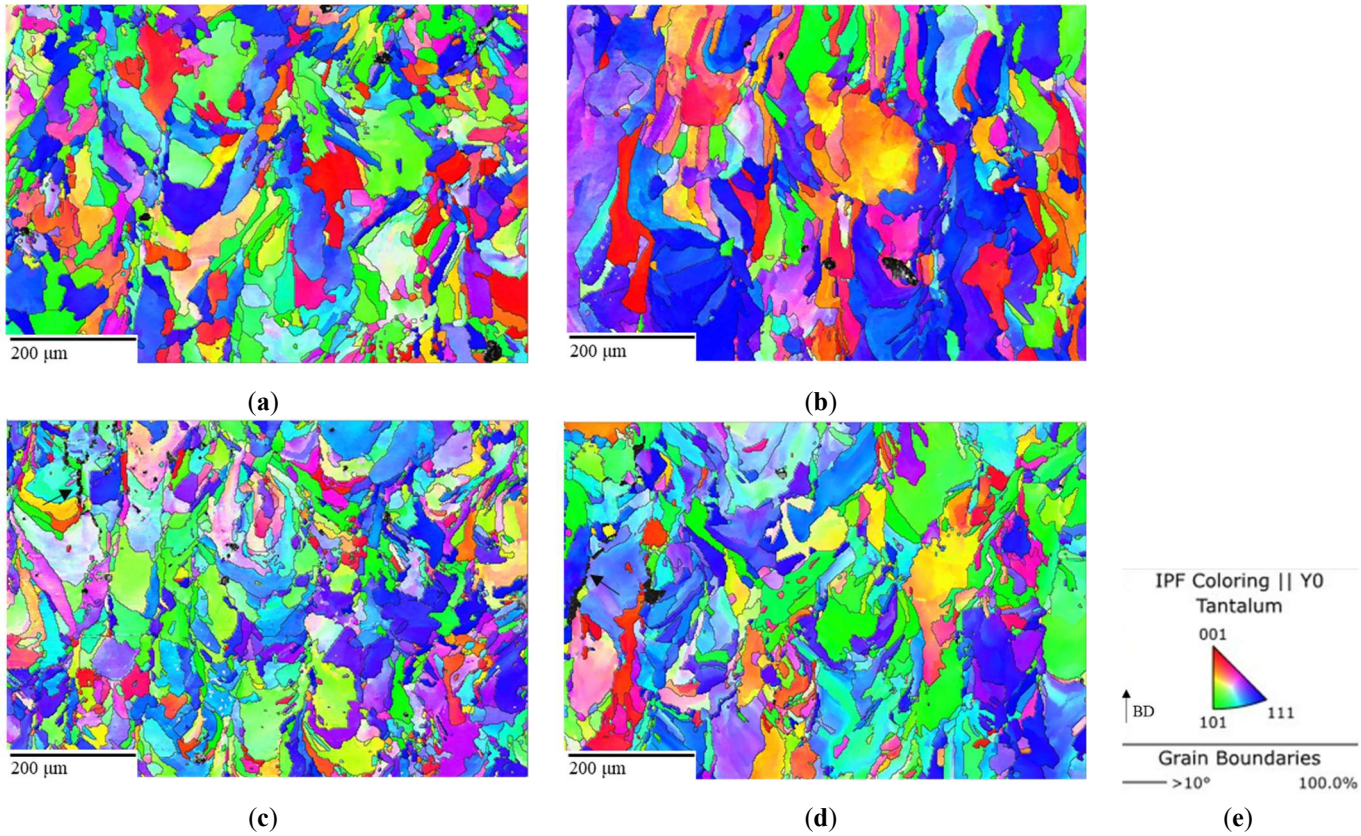

Figure 6. EBSD inverse pole figure (IPF) color maps obtained with 2 µm step width of the PBF-LB/M samples: (**a**) pure Ta, (**b**) Ta-2.5W, (**c**) Ta-5W, (**d**) Ta-7.5W. The IPF are color coded according to the key depicted in (**e**) parallel to Y direction which is the building direction (BD). High-angle (>10°) grain boundaries are indicated in a light greyish color. Black areas represent defects (voids, cracks), the latter of which are indicated by arrows.

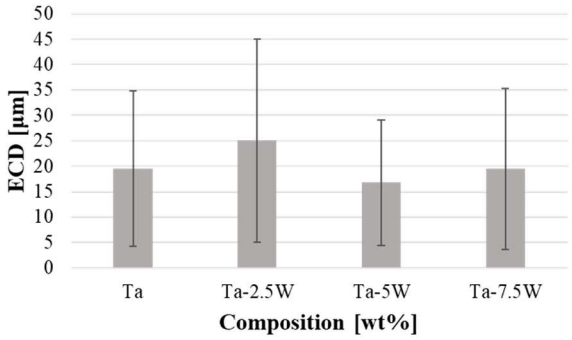

Figure 7. Grain sizes for investigated sites determined by grain reconstruction, representing the equivalent circle diameter (ECD). The respective threshold for analysis was set to ≥10° misorientation. The combined number of measured grains from the different investigated sites, excluding cut grains at image borders, was 716 (Ta), 626 (Ta-2.5W), 3017 (Ta-5W) and 1246 (Ta-7.5W).

The determined grain sizes show a considerable variation, and within the range of the standard deviation, no significant differences can be observed between the samples. From this, it can be concluded that the tungsten content does not have a significant influence on the grain size within the limits of the measurement capabilities.

In the XRD measurements (Figure 8), all samples exhibited strong peaks indicative of pure tantalum or a tantalum-tungsten solid solution. However, a rightward shift of the peaks (detailed in Figure 8b) was observed with increasing tungsten content, suggesting a change in the size of the tantalum lattice by incorporation of tungsten atoms. No significant matches were found with the expected Ta_2O_5 (cf. Figure 5).

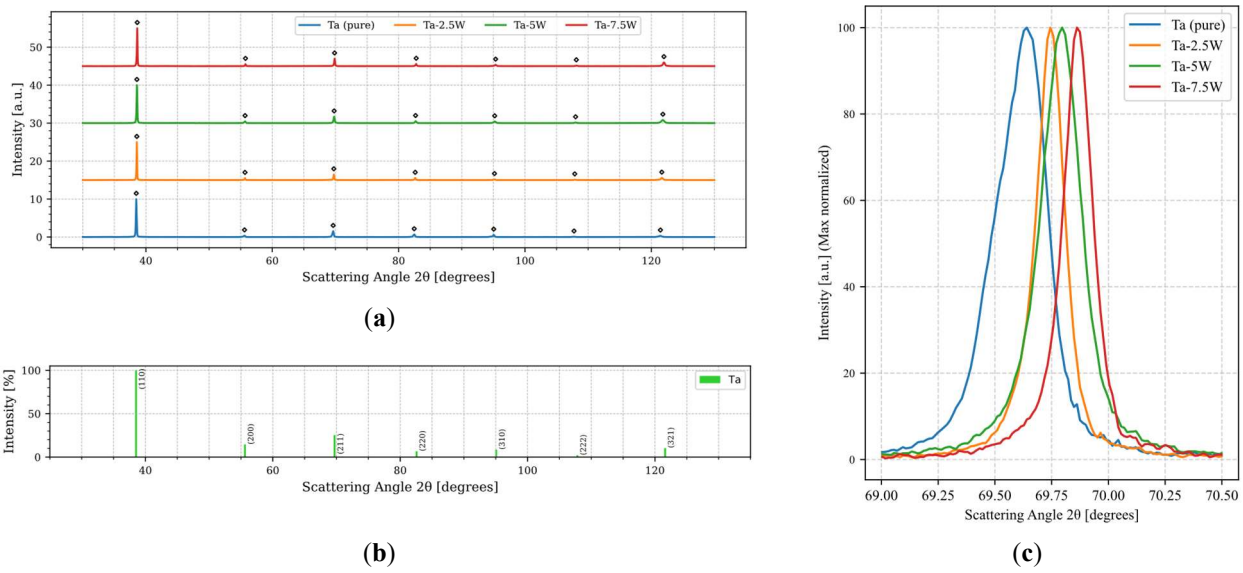

Figure 8. Diffractograms of the three alloys and pure tantalum samples (**a**) with peak markers corresponding to reference standards [54] (**b**). The respective peak positions for pure Ta are indicated by diamond markers. In panel (**c**), enlarged views of the overlapping peaks around 69.7° are presented to better illustrate the observed peak shifts.

3.3. Microhardness

To determine the microhardness, a grid in the center region of the selected samples was set, covering an area of approx. 3.5 mm × 4 mm (height in build direction) to ensure comparability without measuring regions with apparent defects. An example of this layout for Ta-2.5W is shown in the inset in Figure 9. Depicted values in the diagram represent the mean value of all respective measurements per sample. On average, the Ta-7.5W materials exhibit a considerably higher hardness of 385 ± 31 HV compared to both pure Ta (280 ± 11 HV) and Ta-2.5W (300 ± 48 HV, both Figure 9). Although the differences between the 2.5W and 5W samples (338 ± 36 HV) are visible in the mean values, they must be regarded as statistically insignificant due to the scatter in the data. This is also influenced by the fact that the measured tungsten content in the bulk samples deviates from the intended amounts (see Section 3.2). It can be hypothesized that cracking and defects also affect the measured microhardness. While indents clearly placed within a pore or crack were excluded from the measurement, the increased variation may be associated with these and the occasional presence of oxide and tungsten inclusions.

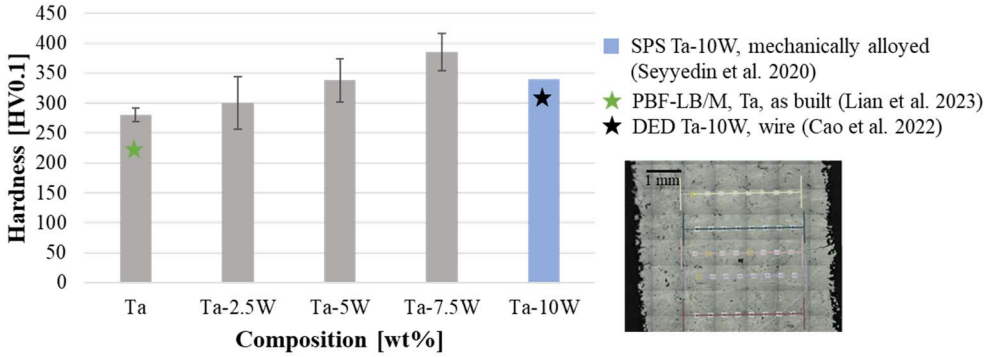

Figure 9. Microhardness measurement results obtained in this study in comparison with selected literature data for similar material. Data for comparison were derived from [16] (SPS Ta-10W), [30] (PBF-LB/M, Ta) and [52] (DED Ta-10W).

4. Discussion

The physical properties of the powder material, including morphology, particle size, surface characteristics, and agglomeration behavior, are known to influence the printed part density significantly and, consequently, the mechanical properties of the final product [55]. Therefore, modifying the powders towards a more spherical shape is expected to enhance flowability during powder bed fusion processes. However, the utilization of mechanical alloyed composite powder (Figure 2) from elemental, non-spherical tantalum and tungsten powder feedstocks for laser powder bed fusion

processing is shown to be feasible for manufacturing dense cuboid specimens (Figure 3). This demonstrates that the powder material produced via mechanical alloying is suitable for application in AM, in line with reports from various research groups that have successfully prepared specimens from elemental powder blends of refractory alloys [56–58].

Printed microstructures exhibit a single solid solution phase, which is expected due to solid solution across the entire binary range of tantalum and tungsten shown by the binary phase diagram [59]. Despite the full solubility of tantalum and tungsten [59], unmolten tungsten particles are sparsely found (Figure 5), which is a phenomenon regularly found in specimens processed from powder blends [60] and demonstrates remaining optimization potential regarding the selection of process parameters. Thus, the full optimization of the AM process and the production of defect-free samples remains a topic for further investigation. In addition to the aforementioned unmolten tungsten particles, isolated oxide inclusions are found within the printed microstructures (Figure 4a). These oxide particles are also found by EDS maps (Figure 5), which are confirmed to be tantalum-rich oxides by with Ta_2O_5 composition by EDS point analysis are believed to stem from the used powder feedstocks due to storage conditions [61]. Sparsely dispersed tantalum oxide particles, e.g., Ta_2O_5 particles, are also found in PBF-LB processing of tantalum by Abdu Aliyu et al. [33]. Thus, oxygen is introduced despite a full argon atmosphere in the mechanical alloying- and laser powder bed fusion process. The oxygen contamination may also explain sparsely found melting defects (Figure 3a) as oxygen deteriorates the wetting behavior of the melt, as described by Tan et al. [36].

As evident from the inverse pole figures obtained from EBSD measurements (Figure 6), the microstructure consists of a fine-grained structure with poly-shaped grains across all examined compositions. This suggests that tungsten has no significant impact on grain formation mechanisms during solidification. From the observed nearly isotropic structure, it can be expected that mechanical properties will also be direction-independent, which is beneficial for most applications. Moreover, no significant impact of tungsten addition on the resulting grain size is recorded (Figure 7), which indicates the incorporation of tungsten into the tantalum lattice by solid solution mechanisms. This is also supported by the shift of the diffraction peaks to higher 2θ values of the (110), (200) and (211) planes (Figure 8), indicating a contraction of the unit cell, possibly due to the substitution of larger tantalum atoms (2.58 Å) [62] by smaller tungsten atoms (2.53 Å) [62]. Similarly, peak shifts were observed in [16] during incorporation of tungsten into tantalum by stepwise mechanical alloying.

However, the microstructure found in the pure tantalum specimens (Figure 6) shows significant differences from pure tantalum specimens manufactured by other research groups with columnar structure in the build direction [2]. One possible explanation may be the oxide particles found, as well as possible additional sub-micron oxide particles, which may act as grain refiner in all manufactured specimens [36]. One other explanation may be in the comparably low volume energy density used in this study (approx. 200 J/mm^3), which may also lead to both reduction of the grain size and change of the grain morphology from columnar to more equiaxed-dominated microstructures. However, the oxide particles are not detected by XRD measurements (Figure 8), which is believed to be due to an insufficient volume fraction of oxide particles in the Ta-W matrix.

Vickers microhardness measurements demonstrate increased hardness with increased tungsten addition (Figure 9). As no significant change in grain size by the addition of tungsten is observed and oxide content is likely to be constant for all specimens, the increase in hardness can be mainly explained by the solid solution hardening mechanism [63] and is in accordance with findings of Browning et al. [17]. The significantly higher hardness values (approx. 280 HV) found for the pure tantalum specimen compared to specimen manufactured by other research groups (approx. 140 HV) [33] further indicate the effect of the found oxides leading to higher material strength by dispersion hardening [35,64]. The high hardness, particularly of Ta-5W and Ta-7.5W specimens may cause the observed severe cracking of the printed specimen (Figure 3c,d). Hence, a higher tungsten content seems to correlate strongly with an increased tendency for crack formation.

5. Conclusions

In this study, non-spherical Ta and Ta-W powders produced by milling were processed by the additive manufacturing process of PBF-LB/M and analyzed regarding overall process feasibility, microstructure and microhardness. The tungsten content has a significant impact on the defects and hardness of the additively manufactured material, while grain size and chemical homogeneity remained predominantly unaffected.

1. The processing of all three as received and milled powders via PBF-LB was possible, resulting in a material density above 99.5%. Cracking could not be suppressed and was found to be most pronounced when adding 7.5 wt% W. The observation is likely linked to the high microhardness of the sample as it suggests that the material's ability to

deform plastically is limited, which can increase the likelihood of cracking. Furthermore, the incorporation of a large amount of tungsten may induce localized stresses within the lattice, further contributing to the material's susceptibility to fracture.

2. All three alloys showed a homogeneous distribution of tungsten in the solid solution, indicating successful alloying. Despite the relatively short milling phase, except for isolated inclusions from unmolten, oxidized particles, no second phases were observed. However, the presence of finely dispersed oxides cannot be excluded.
3. The obtained microstructures were similar and nearly isotropic for all alloys. The addition of tungsten resulted in a measurable increase of hardness while no effect on the grain size varying from 5–45 µm was observed, thus likely indicating solid solution hardening.
4. Hardness values of up to approx. 384 HV0.1 are in accordance with the literature and the smaller grain size of the obtained PBF-LB/M material compared to SPS and DED consolidated material, and suggest the potential for achieving higher strengths compared to previous studies.

In summary, we demonstrated that the processing of an emerging alloy group based on refractory metals is possible with the established process PBF-LB/M starting from low-cost powders and obtained the first indications of promising mechanical properties. Future work will focus on upscaling for in-depth investigation of properties relevant for application and the inclusion of approaches to improve oxidation resistance using, e.g., aluminum, for example, investigated by [9]. The near-net-shape production of components without material loss presents promising prospects for both medical and energy applications of tantalum-based alloys. This is particularly noteworthy as significant progress is being made in the production of pre-alloyed atomized spherical powders suitable for additive manufacturing—an area that has been notably challenging for highly reactive, high-melting materials. For e.g., tungsten, spherical powders have only been produced at great expense using plasma atomization for a long time. Even with recent promising progress, the high demands for purity and flowability keep the costs high. Furthermore, despite the growing demand for high-temperature resistant refractory materials, many alloys and composites are still under development, which complicates upscaling to larger and more cost-effective production quantities. It is expected that the increased variability through simple alloying possibilities, as demonstrated in this study, could significantly contribute to the development of AM-specific alloys, paving the way for more versatile and efficient materials in additive manufacturing applications.

Acknowledgments

We would like to thank Herbert Horn-Solle and Oliver Michels for their well appreciated support in analytics and Thomas Wachowiak for his assistance in material processing and preparation. Additionally, we would like to acknowledge Andreas Weisheit for providing the necessary resources for the initial sample production at Fraunhofer ILT, Aachen.

Author Contributions

Conceptualization, S.-K.R. and M.B.W.; Methodology, S.-K.R., M.B.W. and P.K.; Validation, S.-K.R., M.B.W. and P.K.; Investigation, S.-K.R., M.B.W., F.L., D.N., J.S., P.K.; Resources, S.-K.R. and P.K.; Data Curation, S.-K.R. and P.K.; Writing—Original Draft Preparation, S.-K.R. and M.B.W.; Writing—Review & Editing, F.L., D.N., J.S. and P.K.; Visualization, S.-K.R. and P.K.; Supervision, S.-K.R. and P.K.

Ethics Statement

Not applicable.

Informed Consent Statement

Not applicable.

Data Availability Statement

The datasets generated and analyzed during the current study are available from the corresponding author on reasonable request.

Funding

S.-K.R. gratefully acknowledges financial support from the German Research Foundation (DFG) for the project RI 3559/2-1 (grant no. 536270088).

Declaration of Competing Interest

The authors declare that they have no known competing financial interests or personal relationships that could have appeared to influence the work reported in this paper.

References

1. Oh J, Ishimoto T, Sun S-H, Nakano T. Crystallographic texture formation of pure tantalum by selective laser melting method. *J. Smart. Proc.* **2019**, *8*, 151–154. doi:10.7791/jspmee.8.151.
2. Song C, Deng Z, Zou Z, Liu L, Xu K, Yang Y. Pure tantalum manufactured by laser powder bed fusion: Influence of scanning speed on the evolution of microstructure and mechanical properties. *Int. J. Refract. Met. Hard Mater.* **2022**, *107*, 105882. doi:10.1016/j.ijrmhm.2022.105882.
3. Zhou L, Chen J, Li C, He J, Li W, Yuan T, et al. Microstructure tailoring to enhance strength and ductility in pure tantalum processed by selective laser melting. *Mater. Sci. Eng. A* **2020**, *785*, 139352. doi:10.1016/j.msea.2020.139352.
4. Thijs L, Montero Sistiaga ML, Wauthle R, Xie Q, Kruth J-P, van Humbeeck J. Strong morphological and crystallographic texture and resulting yield strength anisotropy in selective laser melted tantalum. *Acta Mater.* **2013**, *61*, 4657–4668. doi:10.1016/j.actamat.2013.04.036.
5. Zhou L, Yuan T, Li R, Tang J, Wang G, Guo K. Selective laser melting of pure tantalum: Densification, microstructure and mechanical behaviors. *Mater. Sci. Eng. A* **2017**, *707*, 443–451. doi:10.1016/j.msea.2017.09.083.
6. Shi Q, Mao X, Tan C, Ding C, Liu X. Microstructure and mechanical properties of selective laser melted pure tantalum using radio frequency plasma spheroidized powder. *Rare Met. Mater. Eng.* **2020**, *49*, 4023–4030. doi:10.12442/j.issn.1002-185X.2021.49.12.40234030.
7. Sungail C, Abid AD. Additive manufacturing of tantalum—A study of chemical and physical properties of printed tantalum. *Met. Powder Rep.* **2020**, *75*, 28–33. doi:10.1016/j.mprp.2019.03.001.
8. Luo Y, Bi M, Cai H, Hu C, Wei Y, Chen L, et al. Influence of crystal planes on corrosion behavior of tantalum: Experimental and first-principles study. *Int. J. Electrochem. Sci.* **2022**, *17*, 220314. doi:10.20964/2022.03.18.
9. Li J, Chen Y, Li Y, Bai Z, Wang K. Influence of aluminium addition on oxidation resistance of Ta-W alloy. *Powder Met.* **2019**, *62*, 322–330. doi:10.1080/00325899.2019.1662559.
10. Wauthle R, van der Stok J, Yavari SA, van Humbeeck J, Kruth J-P, Zadpoor AA, et al. Additively manufactured porous tantalum implants. *Acta Biomater.* **2015**, *14*, 217–225. doi:10.1016/j.actbio.2014.12.003.
11. Yang J, Jin X, Gao H, Zhang D, Chen H, Zhang S, et al. Additive manufacturing of trabecular tantalum scaffolds by laser powder bed fusion: Mechanical property evaluation and porous structure characterization. *Mater. Charact.* **2020**, *170*, 110694. doi:10.1016/j.matchar.2020.110694.
12. Gao H, Jin X, Yang J, Zhang D, Zhang S, Zhang F, et al. Porous structure and compressive failure mechanism of additively manufactured cubic-lattice tantalum scaffolds. *Mater. Today Adv.* **2021**, *12*, 100183. doi:10.1016/j.mtadv.2021.100183.
13. Chen W, Yang J, Kong H, Helou M, Zhang D, Zhao J, et al. Fatigue behaviour and biocompatibility of additively manufactured bioactive tantalum graded lattice structures for load-bearing orthopaedic applications. *Mater. Sci. Eng. C* **2021**, *130*, 112461. doi:10.1016/j.msec.2021.112461.
14. Kim Y, Kim E-P, Noh J-W, Lee S-H, Kwon Y-S, Oh I-S. Fabrication and mechanical properties of powder metallurgy tantalum prepared by hot isostatic pressing. *Int. J. Refract. Met. Hard Mater.* **2015**, *48*, 211–216. doi:10.1016/j.ijrmhm.2014.09.012.
15. Jakubowicz J, Adamek G, Sopata M, Koper JK, Kachlicki T, Jarzebski M. Microstructure and electrochemical properties of refractory nanocrystalline tantalum-based alloys. *Int. J. Electrochem. Sci.* **2018**, *13*, 1956–1975. doi:10.20964/2018.02.67.
16. Seyyedin S, Zangi H, Bozorgmehr M, Ghasemi B, Tavallaei MM, Adib S. The effect of mechanical alloying time on the microstructural and mechanical properties of spark plasma sintered Ta–10W. *Mater. Sci. Eng. A* **2020**, *798*, 140024. doi:10.1016/j.msea.2020.140024.
17. Browning PN, Alagic S, Carroll B, Kulkarni A, Matson L, Singh J. Room and ultrahigh temperature mechanical properties of field assisted sintered tantalum alloys. *Mater. Sci. Eng. A* **2017**, *680*, 141–151. doi:10.1016/j.msea.2016.09.067.
18. Ma G, Wei Z, Wu G, Mao X. The microstructure and strength of a tantalum alloy: Influence of temperature. *Mater. Sci. Eng. A* **2023**, *880*, 145312. doi:10.1016/j.msea.2023.145312.
19. Iveković A, Omidvari N, Vrancken B, Lietaert K, Thijs L, Vanmeensel K, et al. Selective laser melting of tungsten and tungsten alloys. *Int. J. Refract. Met. Hard Mater.* **2018**, *72*, 27–32. doi:10.1016/j.ijrmhm.2017.12.005.
20. Guo M, Liu K, Sun J, Gu D. Laser powder bed fusion of a novel nano-modified tungsten alloy with refined microstructure and enhanced strength. *Mater. Sci. Eng. A* **2022**, *843*, 143096. doi:10.1016/j.msea.2022.143096.
21. Seyam MS, Koshy P, Elbestawi MA. Laser powder bed fusion of unalloyed tungsten: A review of process, structure, and properties relationships. *Metals* **2022**, *12*, 274. doi:10.3390/met12020274.

22. Xue J, Feng Z, Tang J, Tang C, Zhao Z. Selective laser melting additive manufacturing of tungsten with niobium alloying: Microstructure and suppression mechanism of microcracks. *J. Alloys Compd.* **2021**, *874*, 159879. doi:10.1016/j.jallcom.2021.159879.
23. Rebesan P, Bonesso M, Gennari C, Dima R, Pepato A, Vedani M. Tungsten fabricated by laser powder bed fusion. *BHM* **2021**, *166*, 263–269. doi:10.1007/s00501-021-01109-y.
24. Faidel D, Jonas D, Natour G, Behr W. Investigation of the selective laser melting process with molybdenum powder. *Addit. Manuf.* **2015**, *8*, 88–94. doi:10.1016/j.addma.2015.09.002.
25. Braun J, Kaserer L, Staikovic J, Leitz K-H, Tabernig B, Singer P, et al. Molybdenum and tungsten manufactured by selective laser melting: Analysis of defect structure and solidification mechanisms. *Int. J. Refract. Met. Hard Mater.* **2019**, *84*, 104999. doi:10.1016/j.ijrmhm.2019.104999.
26. Alinejadian N, Wang P, Kollo L, Prashanth KG. Selective laser melting of commercially pure molybdenum by laser rescanning. *3D Print. Addit. Manuf.* **2022**, *10*, 785–791. doi:10.1089/3dp.2021.0265.
27. Kaserer L, Braun J, Staikovic J, Leitz K-H, Tabernig B, Singer P, et al. Fully dense and crack free molybdenum manufactured by selective laser melting through alloying with carbon. *Int. J. Refract. Met. Hard Mater.* **2019**, *84*, 105000. doi:10.1016/j.ijrmhm.2019.105000.
28. Griemsmann T, Abel A, Hoff C, Hermsdorf J, Weinmann M, Kaierle S. Laser-based powder bed fusion of niobium with different build-up rates. *Int. J. Adv. Manuf. Techn.* **2021**, *114*, 305–317. doi:10.1007/s00170-021-06645-y.
29. Chen J, Ding W, Tao Q, Ma C, Zhang C, Chen G, et al. Laser powder bed fusion of a Nb-based refractory alloy: Microstructure and tensile properties. *Mater. Sci. Eng. A* **2022**, *843*, 143153. doi:10.1016/j.msea.2022.143153.
30. Lian F, Chen L, Wu C, Zhao Z, Tang J, Zhu J. Selective laser melting additive manufactured tantalum: Effect of microstructure and impurities on the strengthening-toughing mechanism. *Materials* **2023**, *16*, 3161. doi:10.3390/ma16083161.
31. Valentino GM, Banerjee A, Lark A, Barr CM, Myers SH, McCue ID. Influence of laser processing parameters on the density-ductility tradeoff in additively manufactured pure tantalum. *Addit. Manuf. Lett.* **2023**, *4*, 100117. doi:10.1016/j.addlet.2022.100117.
32. Livescu V, Knapp CM, Gray GT, Martinez RM, Morrow BM, Ndefru BG. Additively manufactured tantalum microstructures. *Materialia* **2018**, *1*, 15–24. doi:10.1016/j.mtla.2018.06.007.
33. Abdu Aliyu AA, Poungsiri K, Shinjo J, Panwisawas C, Reed RC, Puncreobutr C, et al. Additive manufacturing of tantalum scaffolds: Processing, microstructure and process-induced defects. *Int. J. Refract. Met. Hard Mater.* **2023**, *112*, 106132. doi:10.1016/j.ijrmhm.2023.106132.
34. Zhang Y, Aiyiti W, Du S, Jia R, Jiang H. Design and mechanical behaviours of a novel tantalum lattice structure manufactured by SLM. *Virt. Phys. Prototyp.* **2023**, *18*, e2192702. doi:10.1080/17452759.2023.2192702.
35. Song C, Deng Z, Chen J, Yang Z, Zou Z, Liu L, et al. Study on the influence of oxygen content evolution on the mechanical properties of tantalum powder fabricated by laser powder bed fusion. *Mater. Charact.* **2023**, *205*, 113235. doi:10.1016/j.matchar.2023.113235.
36. Tan C, Shi Q, Li K, Khanlari K, Liu X. Effect of oxygen content of tantalum powders on the characteristics of parts processed by laser powder bed fusion. *Int. J. Refract. Met. Hard Mater.* **2023**, *110*, 106008. doi:10.1016/j.ijrmhm.2022.106008.
37. Du J, Ren Y, Zhang M, Liang L, Chen C, Zhou K, et al. Improving the microstructure and mechanical properties of laser powder bed fusion-fabricated tantalum by high laser energy density. *Mater. Lett.* **2023**, *333*, 133547. doi:10.1016/j.matlet.2022.133547.
38. Guo Y, Chen C, Wang Q, Cao Y, Wu C, Zhou K. Microstructural evolution and mechanical behavior of additively manufactured tantalum produced by electron beam powder bed fusion. *Int. J. Refract. Met. Hard Mater.* **2023**, *110*, 106046. doi:10.1016/j.ijrmhm.2022.106046.
39. Guo Y, Chen C, Pan YM, Wang QB, Wu C, Zhou KC. Influence of pore structures on deformation behavior and mechanical properties of porous tantalum scaffolds fabricated by electron beam powder bed fusion. *Trans. Nonferrous Met. Soc. China* **2023**, *33*, 3725–3738. doi:10.1016/S1003-6326(23)66366-6.
40. Marinelli G, Martina F, Ganguly S, Williams S. Microstructure, hardness and mechanical properties of two different unalloyed tantalum wires deposited via wire + arc additive manufacture. *Int. J. Refract. Met. Hard Mater.* **2019**, *83*, 104974. doi:10.1016/j.ijrmhm.2019.104974.
41. Guan B, Xu M, Yang X, Zhou Y, Li C, Ji Y, et al. Microstructure and strengthening mechanisms of tantalum prepared using laser melting deposition. *Int. J. Refract. Met. Hard Mater.* **2022**, *103*, 105773. doi:10.1016/j.ijrmhm.2021.105773.
42. Jafarlou DM, Sousa BC, Gleason MA, Ferguson G, Nardi AT, Cote DL, et al. Solid-state additive manufacturing of tantalum using high-pressure cold gas-dynamic spray. *Addit. Manuf.* **2021**, *47*, 102243. doi:10.1016/j.addma.2021.102243.
43. Yu D, Bi X, Xing L, Zhang Q. Microstructural evolution and mechanical properties of spark plasma sintering of tantalum-tungsten alloys. *Metals* **2023**, *13*, 533. doi:10.3390/met13030533.
44. Sopata M, Siwak P, Adamek G, Jakubowicz J. The mechanical properties of the novel nanocrystalline refractory tantalum alloys. *Prot. Met. Phys. Chem. Surf.* **2020**, *56*, 759–765. doi:10.1134/S2070205120040231.

45. Buckman RW, Jr. Development of high-strength-fabricable tantalum-base alloys. *MRS Online Proc. Libr.* **1993**, *322*, 329–339. doi:10.1557/PROC-322-329.
46. Ma J, Guo X, Xue H, Pan K, Liu C, Pang H. Niobium/tantalum-based materials: Synthesis and applications in electrochemical energy storage. *Chem. Eng. J.* **2020**, *380*, 122428. doi:10.1016/j.cej.2019.122428.
47. Hancock D, Homfray D, Porton M, Todd I, Wynne B. Refractory metals as structural materials for fusion high heat flux components. *J. Nucl. Mater.* **2018**, *512*, 169–183. doi:10.1016/j.jnucmat.2018.09.052.
48. Nemat-Nasser S, Kapoor R. Deformation behavior of tantalum and a tantalum tungsten alloy. *Int. J. Plast.* **2001**, *17*, 1351–1366. doi:10.1016/S0749-6419(00)00088-7.
49. Sopata M, Sadej M, Jakubowicz J. High temperature resistance of novel tantalum-based nanocrystalline refractory compounds. *J. Alloys Compd.* **2019**, *788*, 476–484. doi:10.1016/j.jallcom.2019.02.230.
50. Yukawa H, Nambu T, Matsumoto Y. Ta-W Alloy for Hydrogen Permeable Membranes. *Mater. Trans.* **2011**, *52*, 610–613. doi:10.2320/matertrans.MA201007.
51. Li X, Wan C, Li H, Zhao R, Ju X. Towards understanding the trapping, migration and clustering of He atoms in W–Ta alloy. *J. Nucl. Mater.* **2021**, *554*, 153095. doi:10.1016/j.jnucmat.2021.153095.
52. Cao J, Kong L, Chen Y, Zhang Z, Liang X, Xia M, et al. Laser metal deposition of Ta-10W alloy based on annular laser cladding with internal wire feeding. *J. Phys. Conf. Ser.* **2022**, *2285*, 012002. doi:10.1088/1742-6596/2285/1/012002.
53. Wang X, Wang D, Zhang Y, Li P, Tan Y, Liu B. Characterization of microstructure and mechanical properties of Ta-10W alloy manufactured by laser powder bed fusion. *Int. J. Refract. Met. Hard Mater.* **2024**, *122*, 106728. doi:10.1016/j.ijrmhm.2024.106728.
54. Smirnov YM, Finkel VA. Crystal structure of tantalum, niobium, and vanadium at 110–400 k. *Sov. Phys. —JETP* **1966**, *22*, 750–753.
55. Muthuswamy P. Influence of powder characteristics on properties of parts manufactured by metal additive manufacturing. *Lasers Manuf. Mater. Process.* **2022**, *9*, 312–337. doi:10.1007/s40516-022-00177-3.
56. Kim YS, Goekcekaya O, Matsugaki A, Ozasa R, Nakano T. Laser energy-dependent processability of non-equiatomic TiNbMoTaW high-entropy alloy through in-situ alloying of elemental feedstock powders by laser powder bed fusion. *Materialia* **2024**, *38*, 102241. doi:10.1016/j.mtla.2024.102241.
57. Jobes D, Rubio-Ejchel D, Lopez L, Jenkins W, Sundar A, Tandoc C, et al. Computationally guided alloy design and microstructure-property relationships for non-equiatomic Ti–Zr–Nb–Ta–V–Cr alloys with tensile ductility made by laser powder bed fusion. *Mater. Sci. Eng. A* **2024**, *911*, 146922. doi:10.1016/j.msea.2024.146922.
58. Xu J, Qin M, Du S, Kumar P, Zhu J, Jia Y, et al. Enhancing the strength and plasticity of laser powder bed fused NbMoTaW refractory high-entropy alloy via Ti alloying. *J. Alloys Compd.* **2024**, *1001*, 175043. doi:10.1016/j.jallcom.2024.175043.
59. Jiang D, Wang Q, Hu W, Wei Z, Tong J, Wan H. The effect of tantalum (Ta) doping on mechanical properties of tungsten (W): A first-principles study. *J. Mater. Res.* **2016**, *31*, 3401–3406. doi:10.1557/jmr.2016.358.
60. Strauch AL, Uhlenwinkel V, Steinbacher M, Großwendt F, Röttger A, Chereh AB, et al. Comparison of the processability and influence on the microstructure of different starting powder blends for laser powder bed fusion of a $Fe_{3.5}Si_{1.5}C$ alloy. *Metals* **2021**, *11*, 1107. doi:10.3390/met11071107.
61. Riener K, Oswald S, Winkler M, Leichtfried GJ. Influence of storage conditions and reconditioning of AlSi10Mg powder on the quality of parts produced by laser powder bed fusion (LPBF). *Addit. Manuf.* **2021**, *39*, 101896. doi:10.1016/j.addma.2021.101896.
62. Rahm M, Hoffmann R, Ashcroft NW. Atomic and ionic radii of elements 1–96. *Chem. Eur. J.* **2016**, *22*, 14625–14632. doi:10.1002/chem.201602949.
63. Zhao R, Chen C, Wang W, Cao T, Shuai S, Xu S, et al. On the role of volumetric energy density in the microstructure and mechanical properties of laser powder bed fusion Ti-6Al-4V alloy. *Addit. Manuf.* **2022**, *51*, 102605. doi:10.1016/j.addma.2022.102605.
64. Wilms MB, Rittinghaus S-K, Goßling M, Gökce B. Additive manufacturing of oxide-dispersion strengthened alloys: Materials, synthesis and manufacturing. *Progr. Mater. Sci.* **2023**, *133*, 101049. doi:10.1016/j.pmatsci.2022.101049.